NASA Technical Paper 2540

April 1986

Site Selection and Directional Models of Deserts Used for ERBE Validation Targets

W. Frank Staylor

NASA

NASA
Technical
Paper
2540

1986

Site Selection and Directional Models of Deserts Used for ERBE Validation Targets

W. Frank Staylor

Langley Research Center
Hampton, Virginia

National Aeronautics
and Space Administration

**Scientific and Technical
Information Branch**

Summary

Broadband shortwave and longwave radiance measurements obtained from the Nimbus 7 Earth Radiation Budget scanner were used to develop reflectance and emittance models for the Sahara, Gibson, and Saudi Deserts. These deserts will serve as in-flight validation targets for the Earth Radiation Budget Experiment being flown on the Earth Radiation Budget Satellite and two National Oceanic and Atmospheric Administration polar satellites. The directional reflectance model derived for the deserts was a function of the sum and product of the cosines of the solar and viewing zenith angles, and thus reciprocity existed between these zenith angles. The emittance model was related by a power law of the cosine of the viewing zenith angle.

Introduction

Three Earth Radiation Budget Experiment (ERBE) missions will be launched during 1984–1986 to study the regional, zonal, and global radiation properties of the Earth. To meet the stringent accuracy goals set for ERBE, the satellite orbits must permit frequent coverage of the entire globe, and the instruments must provide high radiometric accuracy. Coverage errors are basically fixed by the number of satellites and their orbits (Harrison et al. 1983), while radiometric errors are determined by the design of the sensors and the degree to which their calibrations are known in flight. All the ERBE instruments were extensively calibrated and characterized in a ground test facility; nonetheless, onboard calibration systems were provided to recalibrate the sensors and to validate their long-term stability in flight. A more complete description of the ERBE sensors and their ground and onboard calibration systems is given by Barkstrom (1984).

The need for in-flight calibration became apparent in the early 1960's when radiometers exposed to the harsh space environment often degraded at alarming rates and in unknown manners. Consequently, onboard calibration systems were added that generally took the form of solar diffusers, incandescent lamps, or both for shortwave sensors and temperature-controlled blackbodies for longwave sensors (Williamson 1977). Unfortunately, in-flight calibration systems can also degrade, fail, or become unusable for numerous reasons. Futhermore, their applicability is questionable because they are usually activated in special calibration sequences that are substantially different from their operational Earth-viewing modes.

One in-flight calibration technique that eliminates some of the problems encountered with onboard calibration systems is the use of operational measurements that view natural Earth targets as calibration values. Selected Earth sites, in effect, become the solar diffuser plates and thermal blackbodies. For instance, the bright gypsum sands and the nearby dark lava flows at White Sands, New Mexico, are occasionally used as relative comparison targets for satellite sensors. The primary use of such sites for the ERBE missions will be to serve as a long-term stable target for calibrations and for comparisons of measurements (1) among the three ERBE missions, (2) between different ERBE instruments on a given mission, (3) between ERBE results and those of previous missions (Nimbus 2 and 3, medium resolution infrared radiometer; Nimbus 6 and 7, Earth Radiation Budget (ERB) scanner), and (4) between ERBE results and those of future radiation budget missions.

The present paper is concerned with, first, the selection of target sites amenable to the ERBE missions, and then, the directional modeling of the broadband reflection and emission properties of those sites. For a number of reasons given later, all the selected sites were deserts: Sahara, Gibson, and Saudi. Nimbus 7 ERB scanner data were used to develop the cloud-free desert models, and comparisons are made between the Nimbus 6 and 7 ERB results for the Saudi Desert.

Symbols

A	albedo
C_{LW}, C_{SW}	longwave and shortwave azimuthal phase function constants
E_{LW}	longwave radiant exitance, W-m^{-2}
F_{LW}, F_{SW}	measured longwave and shortwave radiant fluxes, W-m^{-2}
L_{LW}, L_{SW}	broadband longwave and shortwave radiance measurements, W-m^{-2}-sr^{-1}
$\bar{L}_{LW}$	directional emittance, W-m^{-2}-sr^{-1} (see eq. (9))
$\bar{L}_{LW,\theta}$	directional emittance to zenith angle θ, W-m^{-2}-sr^{-1}
M	longwave regression coefficient (see eq. (10))
N	shortwave regression coefficient (see eq. (3))
P_{LW}, P_{SW}	longwave and shortwave azimuthal phase functions

R	bidirectional reflectance (see eq. (1))
$\overline{R}$	directional reflectance (see eq. (2))
$R_{\min}$	minimum bidirectional reflectance
r_a, r_s	Earth radii to top of atmosphere and to satellite
S	Earth-Sun distance-corrected solar flux, W-m^{-2}
S_0	mean Earth-Sun distance solar flux, 1376 W-m^{-2}
U, U_0	cosines of viewing and solar zenith angles, respectively
$U_{\max}$	cosine of maximum viewing zenith angle observed by MFOV sensor
V, V_0	sines of viewing and solar zenith angles, respectively
X	$UU_0/(U+U_0)$ or $(\sec\theta + \sec\theta_0)^{-1}$
Y	$\overline{R}UU_0$ or RUU_0/P_{SW}
Y_0, Y_1	shortwave regression coefficients (see eq. (3))
α	cone angle of MFOV sensor
$\alpha_{\max}$	maximum cone angle of MFOV sensor
β	clock angle of MFOV sensor
γ	scattering angle (see eq. (4))
θ, θ_0	viewing zenith angle and solar zenith angle, respectively
σ	standard error of estimate for Y
ϕ	solar azimuth angle

Abbreviations:

AVHRR	advanced very high resolution radiometer
ERB	Earth Radiation Budget (sensors onboard Nimbus 6 and 7)
ERBE	Earth Radiation Budget Experiment
ERBS	Earth Radiation Budget Satellite
HIRS	high resolution infrared radiation sounder
IFOV	instantaneous field of view
LST	local standard time
MFOV	medium field of view
NFOV	narrow field of view
NOAA F,G	National Oceanic and Atmospheric Administration Tiros N-series satellites
WFOV	wide field of view

Site Selection

Required and Desired Site Properties

The rationale for the selection of the present target sites is given below. Certain site properties must be classified as requirements, while others are merely desirable properties.

Stability. The most basic requirement of any target site is that it must provide a stable, predictable radiometric signal when observed from space. A site must offer long-term stability with no appreciable surface changes expected during the period of interest in order for direct comparisons to be made between previous as well as future radiation budget measurements and those for ERBE. Even short-term variances due to ice, snow, wet soil, and vegetation growth, for instance, are undesirable features in that ERBE target sites could be utilized on a daily basis, when cloud-free. Although all areas of the globe experience some degree of cloudiness, strong weighting was given to those sites where cloudiness and precipitation are minimal.

High albedo/low solar zenith angle. All the ERBE shortwave sensors view space and/or the dark side of the Earth during flight and thus experience a zero input condition. The most appropriate additional reference condition would be one near the maximum levels measured during flight, which occur for high-albedo sites at low solar zenith angles. Clouds, ice, and snow have high albedos but do not provide stable, predictable radiometric surfaces. In general, deserts are stable and predictable and have high albedos, and several large deserts are located at low latitudes where the lowest possible solar zenith angles will be experienced by each of the ERBE satellites.

Size. It would be desirable to have target sites for all three of the ERBE sensors, which are the narrow-field-of-view (NFOV) scanner and the medium-field-of-view (MFOV) and wide-field-of-view (WFOV) nonscanners. However, no acceptable site is sufficiently large for the WFOV sensor, which views the entire Earth disc, and its in-flight calibration will rely heavily on the onboard calibration systems. The MFOV sensor views an Earth-central-angle nadir

scene of 10°, and for observations each day, the site must be about 10° in latitude by 36° in longitude. The NFOV scanner has an IFOV of about 3° by 3°, and its target sites could be relatively small. However, scanner measurements will be assembled by regions that are 2.5° in latitude and longitude, which thus become convenient site dimensions. Approximately 20 (limb) to 120 (nadir) NFOV scanner measurements will be obtained from regional sites during each day and night overpass.

Uniformity. There is no requirement that a target site be radiometrically uniform provided that the entire site is sampled during each orbital passage. However, uniformity is certainly a desirable site property in that histograms of the shortwave and longwave radiances (from AVHRR, HIRS, and/or ERBE NFOV) will be used to detect the presence of clouds and, perhaps, wet sand and dust storms. Lambertian or near-Lambertian target sites are desirable in that they can be more accurately modeled.

Potential Areas

Only low-latitude deserts meet all the requirements: long-term stability and predictability, high albedos combined with low solar zenith angles, and large size. Furthermore, most of these deserts are located in northern Africa, the Arabian Peninsula, and central Australia, all of which have low-cloudiness and low-precipitation statistics (Sherr et al. 1968). Nimbus 6 ERB scanner data taken during June 1977 (scanner pointed at nadir) were used to search these large areas for potential target sites. In particular, the search was directed toward finding near-uniform regions that might best serve as NFOV target sites.

Selected Target Sites

The area selected as the MFOV target site is located in the Sahara Desert and is bounded by latitudes 17°N to 27°N and longitudes 3°W to 33°E. This site can generally be characterized as having vast expanses of sand dunes, sand seas, arid gravel, and rock outcroppings with very little moisture or vegetation (Short et al. 1976). Nadir radiances from Nimbus 6 revealed maximum variances of ±20 percent for the entire site, but maximum variances of only ±10 percent for more than 90 percent of the site. Because of solar zenith angle problems, explained later, a second MFOV site was considered which spanned the entire central Australian Continent. This area has large variances (±30 percent) plus seasonal vegetation growth (mostly range grasses) and was not considered acceptable as a target site.

The region selected as the primary NFOV target site is located in the Ar Rab al Khali Basin of the Arabian Peninsula and is bounded by latitudes 20.0°N to 22.5°N and longitudes 50.0°E to 52.5°E. This general area is often referred to as the Arabian Empty Quarter, but because it is located totally within the borders of Saudi Arabia, it will be referred to here as the Saudi Desert. This site is almost entirely sand dunes and sand seas, and the lack of moisture and the saline nature of the sand cause it to be virtually free of all vegetation (Short et al. 1976).

For two opportunities during each 72-day precession cycle of the Earth Radiation Budget Satellite (ERBS), the minimum solar zenith angles for the satellite as it passes over the Saudi and Sahara sites will range from 0° to 45° depending on the time of year (i.e., solar declination). Solar zenith angles will range from 35° to 58° for the NOAA F (1430 LST) and from 55° to 74° for the NOAA G (0800 LST) Sun-synchronous spacecraft as they pass over these sites during the course of a year. While the ranges of solar zenith angles for the ERBS and NOAA F spacecraft are acceptable, the maximum angles for the NOAA G spacecraft, which occur during the fall and winter seasons at the Sahara and Saudi sites, are somewhat large and will not provide the high radiometric values desired for shortwave calibrations. This problem can be alleviated by the addition of sites located in the Southern Hemisphere for use during October through March.

The region selected as an alternate NFOV target site is located in the Gibson Desert of western Australia and is bounded by latitudes 25.0°S to 27.5°S and longitudes 120.0°E to 122.5°E. This site has a mixture of sand dunes, dry salt lakes, rock outcroppings, and arid steppe vegetation (Short et al. 1976). However, after infrequent heavy rains, the lakes temporarily flood, and the sparse vegetation flourishes. These occurrences are undesirable from the present standpoint because they would prevent use of the site until arid conditions returned.

Broadband shortwave, L_{SW} and longwave, L_{LW}, radiance measurements from the Nimbus 6 ERB scanner are presented in figure 1 to illustrate the surface uniformities of the Saudi and Gibson NFOV target sites. These nadir measurements represent 100-km swaths that passed directly across the centers of the sites as the spacecraft coursed northward on daylight passages. The shortwave and longwave radiance variances for these as well as the adjacent swaths (i.e., total coverage) were less than 5 percent for both NFOV sites.

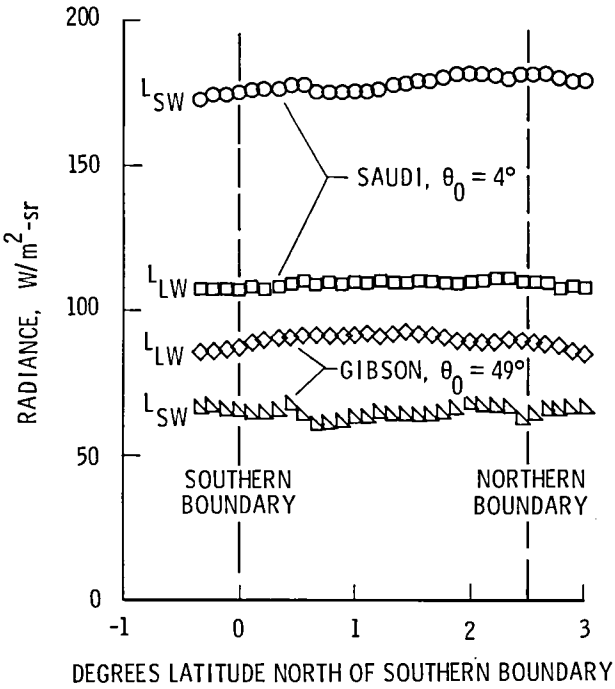

Figure 1. Illustration of uniformity for NFOV scanner sites. Data from Nimbus 6 ERB scanner; $\theta = 6°$; June 1977.

Satellite Measurements

Satellites and Instruments

Radiance measurements from the Nimbus 7 ERB scanner were used for modeling purposes, and they were compared with the Nimbus 6 results for the Saudi Desert. The Nimbus 6 satellite was launched June 12, 1975, to an altitude of 1100 km and an inclination of 100°, and the Nimbus 7 satellite was launched October 24, 1978, to an altitude of 950 km and an inclination of 99°—both into noon, Sun-synchronous orbits.

The ERB scanner had four telescopes, each of which had a broadband shortwave (0.2–4 μm) channel and a broadband longwave (5–50 μm) channel. It scanned from horizon to horizon along the orbital groundtrack and to a zenith angle of 72° in the crosstrack direction. This multiaxis scanning capability provided measurements over a wide range of angular parameters which are particularly useful for directional modeling purposes. At the nadir, the spatial resolution (Nimbus 7) was about 90 km, and it increased to about 250 km at the horizon. A more detailed description of the ERB instrument and its operation is given by Smith et al. (1977).

Data Sets

The data set used to develop the basic desert models consisted of 123 141 pairs of shortwave and longwave radiances from the Sahara Desert measured by the Nimbus 7 ERB scanner from November 1978 to May 1980 (Stowe and Fromm 1983). These data were sorted into 191 ranges of angles, called bins, to provide discrete parameter values for modeling and display. Bins were sorted by viewing zenith angle, θ, azimuth angle, ϕ ($\phi = 0°$ for forward reflection; $\phi = 180°$ for backward reflection), and U_0, cosine of the solar zenith angle. Bin angular ranges are given in table I. For each of the data bins, the bin description (θ, ϕ, U_0), the mean of both L_{SW}/U_0 and L_{LW}, and the bin population were available in tabular form. In addition, the albedo, A, was computed for each of the four U_0 ranges by using a mean Earth-Sun distance solar flux, S_0, of 1376 W/m^2. This data set was compiled and processed under the direction of V. R. Taylor and L. L. Stowe of the National Oceanic and Atmospheric Administration/National Environmental Satellite, Data, and Information Service.

The Nimbus 7 data used to model the Gibson and Saudi Deserts were taken during several days in December 1978 and March, July, and December 1979 when the spacecraft passed near the sites. These measurements were individual shortwave and longwave radiance pairs obtained from within the boundaries of the 2.5° regional sites. The December 1978 through July 1979 data provided maximum, medium, and minimum solar zenith angles at both sites, and the December 1979 data were added primarily for direct comparisons with the December 1978 data to determine whether sensor degradations had occurred during the year. Nimbus 6 data for the Saudi Desert taken during August 1975 (Suttles 1981) were included for comparison with the Nimbus 7 results. Data set populations and angular ranges are given in table II.

Measurements taken with clouds within the instantaneous fields of view of the ERB scanner were eliminated from the Sahara data set by using the window radiances (11 μm) of the temperature-humidity infrared radiometer (THIR, also onboard Nimbus 7) in an editing technique developed by Stowe (1983). Cloudy days were eliminated from the Gibson and Saudi data sets by analyzing the general levels of the ERB L_{SW} and L_{LW} values (overcast) and by requiring continuity in the daily plots of L_{LW} versus θ (partial cloudiness).

Reflectance Model

Sahara Directional Model

Bidirectional reflectance is defined here as

$$R = \frac{\pi L_{SW}}{S U_0} \tag{1}$$

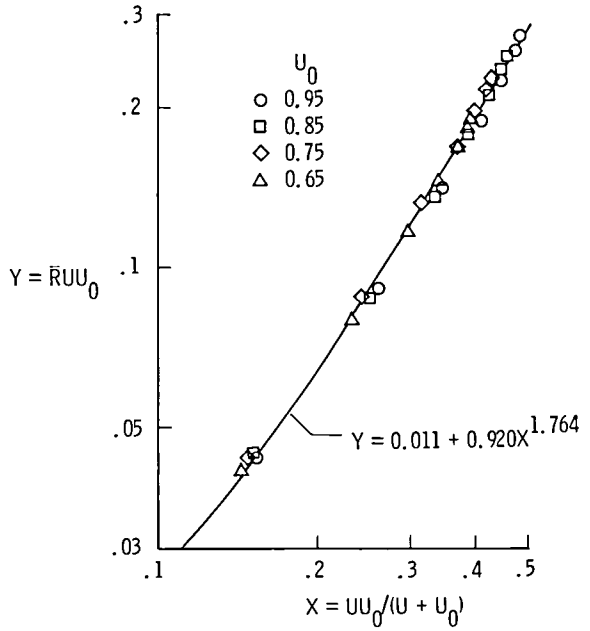

Figure 2. Correlation of directional reflectance for Sahara Desert as a function of viewing and solar zenith angles.

and is a function of θ_0, θ, and ϕ. (S is the distance-corrected solar flux.) Azimuthal dependence is eliminated for the directional reflectance, which is defined as

$$\overline{R} = \frac{1}{\pi}\int_0^{\pi} R\, d\phi \tag{2}$$

Barkstrom (1973), using single-scattering approximations, found that $\overline{R}UU_0$ could be expressed as a function of $UU_0/(U + U_0)$ where $U = \cos\theta$. Staylor (1985) also found these parameters to be useful for the directional modeling of overcast low-, middle-, and high-water clouds and high-ice clouds.

Directional reflectance parameters, $\overline{R}UU_0$, for the Sahara Desert data are presented in figure 2 as a function of $UU_0/(U + U_0)$, which is the inverse of the total atmospheric slant path, $\sec\theta + \sec\theta_0$. The data are well correlated with a curve related by the equation

$$Y = Y_0 + Y_1 X^N \tag{3}$$

where $X = UU_0/(U + U_0)$ and $Y = \overline{R}UU_0$. A general discussion of the technical significance of the regression coefficients Y_0, Y_1, and N is given by Staylor (1985). Briefly, Y_0 accounts for the nonzero radiance due to atmospheric refraction and scattering measured near the terminator ($U_0 = 0, X = 0$). The coefficient Y_1 relates the general brightness level of the surface: 0.1 to 0.2 for clear oceans, 0.2 to 0.5 for soils, 0.6 to 1.1 for deserts, 1.2 to 1.5 for clouds, and 1.8 to 2.4 for snow. The coefficient N has several components, one of which relates the transmission within the surface medium, primarily grains of sand in the present case, and another of which relates the transmission of the atmosphere above the surface.

Azimuthal Phase Function

Directional reflectance is a useful parameter for correlative purposes and for the calculation of albedo. However, during an overflight of a target site, the ERBE NFOV scanner will not observe the site at sufficient azimuth angles for the accurate computation of $\overline{R}$. Therefore, directional reflectance has little direct application to the present task of estimating target radiances unless the site reflectance is isotropic (i.e., $R = \overline{R}$). It is clear that an azimuthal phase function is needed that will convert the modeled $\overline{R}$ values into the required R values. The azimuthally binned Sahara data set was ideally suited to this task.

Staylor (1985) found that the bidirectional reflectances for clouds were well correlated with scattering angle, γ, which can be expressed as

$$\cos\gamma = \sin\theta \sin\theta_0 \cos\phi - \cos\theta \cos\theta_0 \tag{4}$$

where $\gamma = 0°$ is forward scattering, and $\gamma = 180°$ is backward scattering. Plots of R versus γ for constant bin values of θ and θ_0 indicated that the Sahara reflectances behaved in a Rayleigh-like manner and could be approximated as

$$R \approx R_{\min}(1 + C_{SW} \cos^2\gamma) \tag{5}$$

where $R_{\min}$ is a function of θ and θ_0, and C_{SW} is a constant. The azimuthal phase function, P_{SW}, can be expressed as

$$P_{SW} = \frac{R}{\overline{R}} = \frac{1 + C_{SW}(UU_0 - VV_0 \cos\phi)^2}{1 + C_{SW}[(UU_0)^2 + 1/2(VV_0)^2]} \tag{6}$$

where $V = \sin\theta$ and $V_0 = \sin\theta_0$.

Equation (6) indicates that azimuthal anisotropy should peak when the VV_0 term is at its maximum value. Measured values of $R/\overline{R}$ are plotted in figure 3 as a function of γ for six U, U_0 bins which have large VV_0 values (i.e., small values of UU_0). These data are well correlated with a curve generated by equation (6) with mean values of U and U_0, and $C_{SW} = 0.33$.

The azimuthal phase function, as related by equation (6), has several notable features. First, it will accommodate predominately backward-reflecting surfaces ($C_{SW} > 0$) such as the Sahara Desert, predominately forward-reflecting surfaces ($C_{SW} < 0$), and isotropic surfaces ($C_{SW} = 0$). Second, azimuthal dependence is minimal if one or both of the zenith angles are near their nadirs ($VV_0 \approx 0$), which is a generally observed phenomenon. And third, the phase

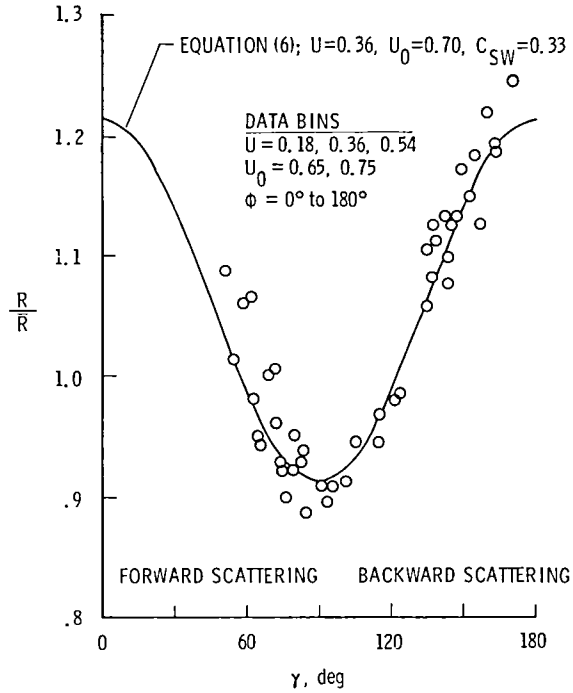

Figure 3. Illustration of Rayleigh-like shape of azimuthal phase function as a function of scattering angle. Data from Sahara Desert for high zenith angles.

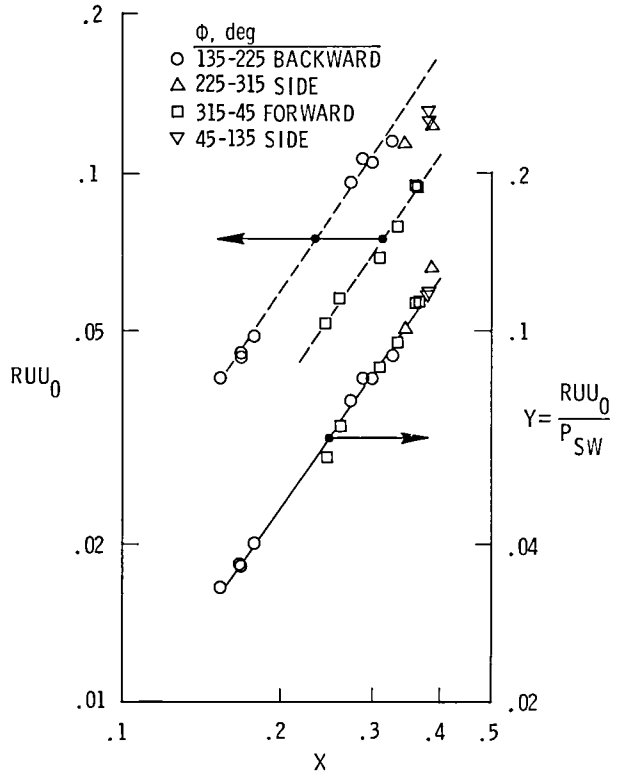

Figure 4. Normalization of bidirectional reflectance for Gibson Desert site, $\theta_0 \approx 50°$, July 1979. Note difference in left and right vertical scales.

function exhibits zenith angle reciprocity, which is discussed in more detail later.

Gibson and Saudi Directional Models

Bidirectional parameters RUU_0 for the Gibson Desert are presented in figure 4 (top, left scale) as a function of X. These data were taken during July 1979, when the noontime solar zenith angle was near its maximum yearly value ($\theta_0 \approx 50°$), and best illustrate the relatively high anisotropy of this target site. The backward-reflecting data lie along the top dashed line, the forward-reflecting data lie along the bottom dashed line, and the side-reflecting data lie between. However, when normalized by the azimuthal phase function, $P_{SW}(C_{SW} = 0.60)$, these data collapse into a single line (bottom, right scale). All the Gibson data for the 4 sampled months are given in figure 5 and are well correlated with a regression curve related by equation (3).

Nimbus 7 Saudi Desert data for the 4 sampled months are presented in figure 6 (top, left scale) as a function of X. Similarly, the Nimbus 6 Saudi data for August 1975 are also given (bottom, right scale). Both data sets were normalized by $P_{SW}(C_{SW} = 0.18)$ and show good agreement with their regression curves. All regression coefficients used for the desert reflection models are listed in table III.

Anisotropic reflection diagrams (i.e., R/A) are given in figure 7 for the Gibson (left) and Saudi (right) Deserts. The diagrams show that both desert sites are predominately back-reflecting, and that the Saudi Desert has the more desired, near-isotropic pattern.

Albedo

Local albedo can be expressed as

$$A = 2\int_0^1 \overline{R}U\,dU \tag{7}$$

which with the substitution of equation (3) becomes

$$A = 2Y_0U_0^{-1} + 2Y_1U_0^{N-1}\int_0^1 \left(\frac{U}{U+U_0}\right)^N dU \tag{8}$$

The albedo curves given in figure 8 were computed from equation (8) with the Nimbus 7 coefficients listed in table III. Bin-integrated albedos for the Sahara Desert (Taylor et al. 1983) are in good agreement with their computed curve. The Saudi site is clearly the brightest of the three deserts, followed by the Sahara, with the Gibson site being the darkest desert.

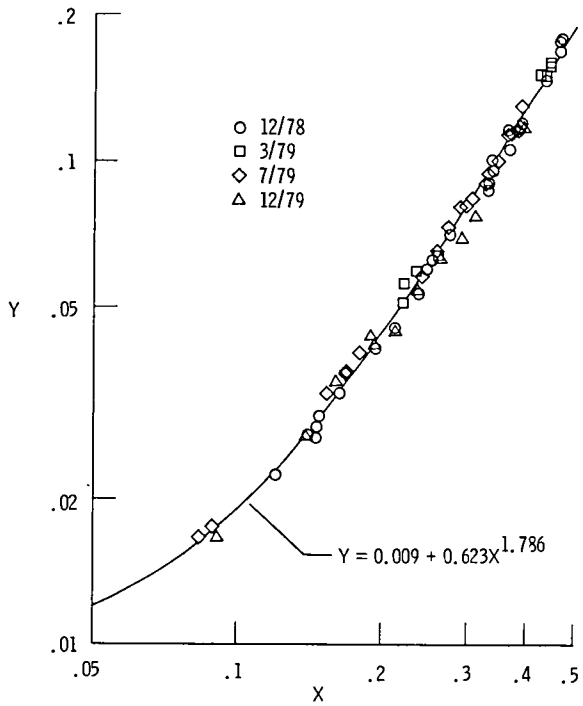

Figure 5. Correlation of directional reflectance for Gibson Desert site as a function of viewing and solar zenith angles.

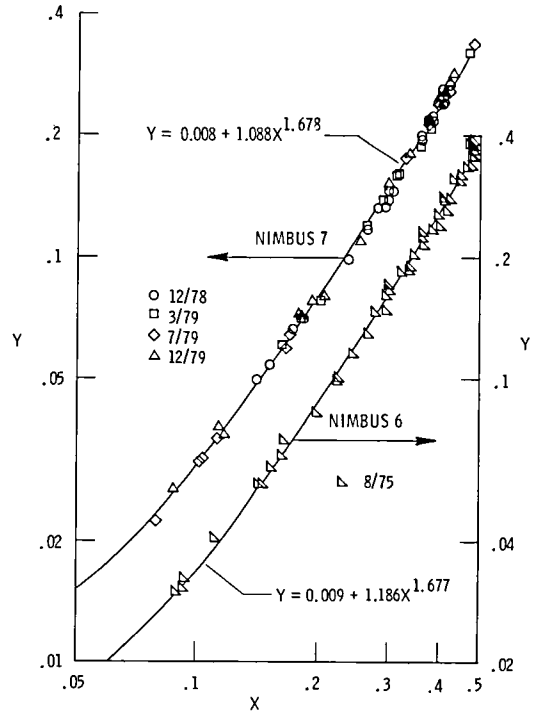

Figure 6. Correlation of Nimbus 7 (left scale) and Nimbus 6 (right scale) directional reflectances for Saudi Desert site.

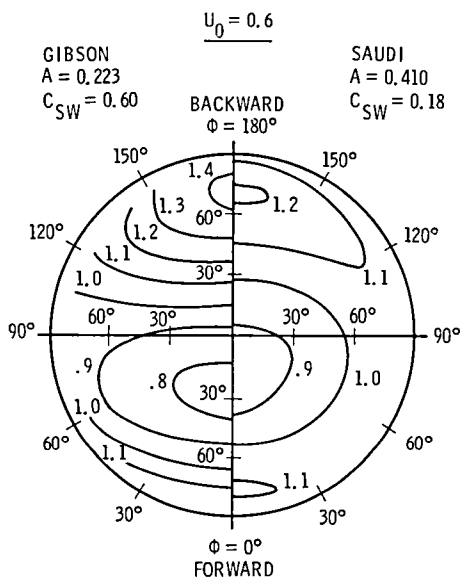

Figure 7. Anisotropic reflectance diagrams (R/A) computed from Gibson and Saudi Desert models. $U_0 = 0.6$.

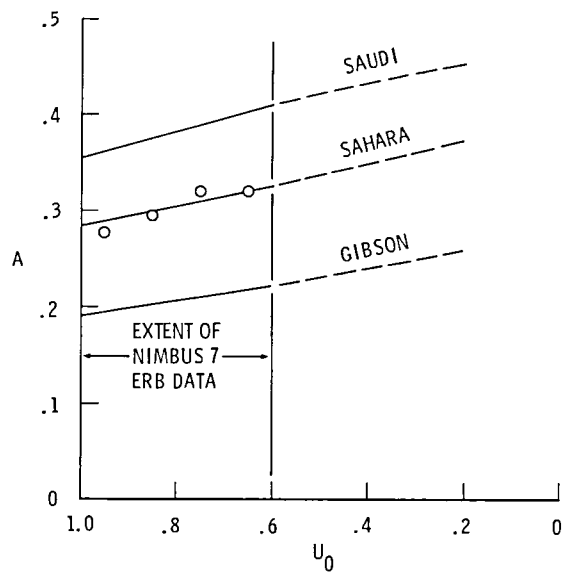

Figure 8. Albedos computed from Saudi, Sahara, and Gibson Desert models. Symbols are bin-integrated values for Sahara Desert from Taylor et al. (1983).

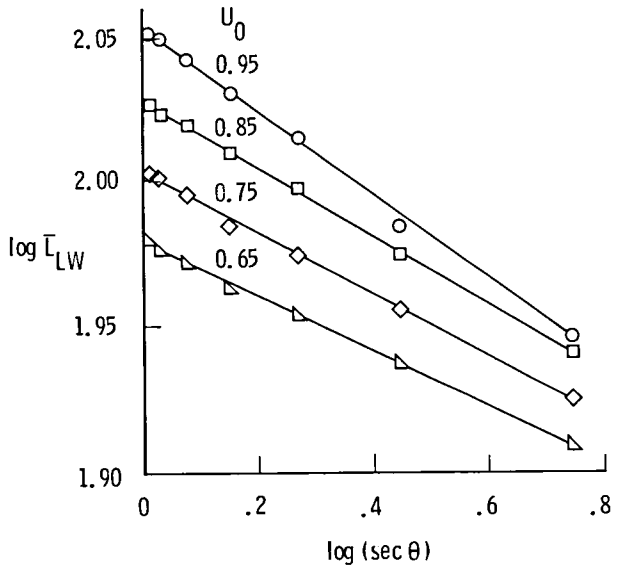

Figure 9. Correlation of limb-darkening with zenith angle for Sahara Desert.

Emittance Model

There was little variation of the emitted longwave radiances with azimuth angle for the Sahara data set, and the directional emittance defined as

$$\bar{L}_{LW} = \frac{1}{\pi}\int_0^{\pi} L_{LW}\, d\phi \qquad (9)$$

was computed for all θ, θ_0 bins. Values of $\bar{L}_{LW}$ plotted in figure 9 versus sec θ on a log-log scale are quite linear for each value of U_0 and can be related as a power law of U as

$$\bar{L}_{LW,\theta} = \bar{L}_{LW,0^\circ}(\sec\theta)^{-M} = \bar{L}_{LW,0^\circ}U^M \qquad (10)$$

Staylor (1985) previously found that this limb-darkening function also applied for overcast clouds.

Initial attempts to model the L_{LW} data for the Gibson and Saudi Deserts in a similar manner were somewhat disappointing. For instance, the Gibson longwave radiances for July 1979 ($\theta_0 \approx 50°$) behaved, on a reduced scale, in a manner very similar to the shortwave reflectances shown in figure 4. Namely, the backward radiances (ϕ = 135° to 225°) were higher and the forward radiances (ϕ = 315° to 45°) were lower than the mean values. It was found that this emission anisotropy could be removed, to a large degree, by an azimuthal phase function, shown below, that was identical in form to that used for the shortwave anisotropy

$$P_{LW} = \frac{L_{LW}}{\bar{L}_{LW}} = \frac{1 + C_{LW}(UU_0 - VV_0\cos\phi)^2}{1 + C_{LW}[(UU_0)^2 + 1/2(VV_0)^2]} \qquad (11)$$

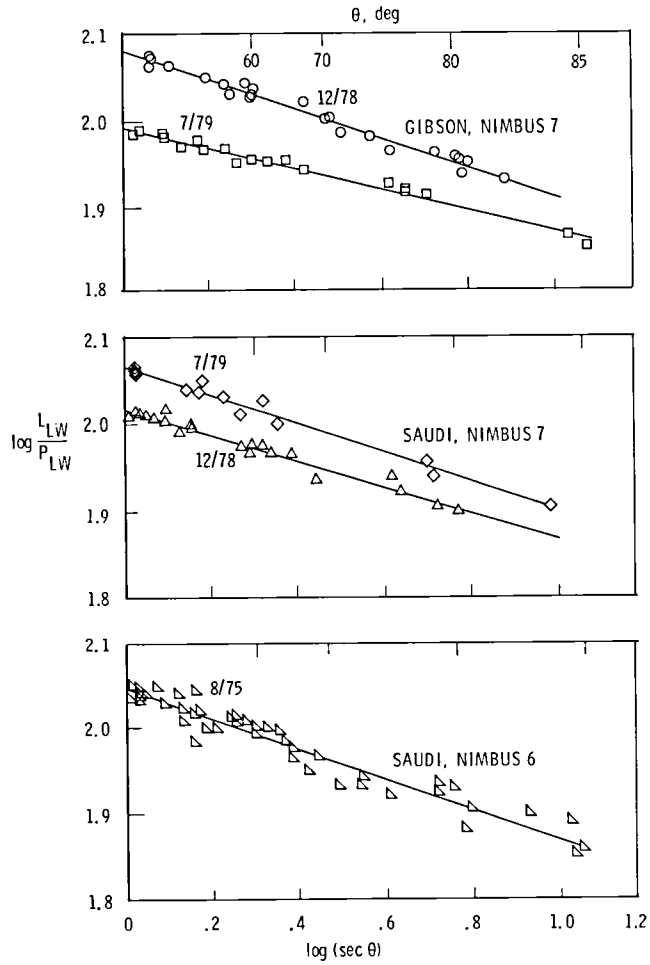

Figure 10. Correlation of limb-darkening with zenith angle for Gibson and Saudi Desert sites.

The normalized longwave radiances, L_{LW}/P_{LW}, for the Gibson and Saudi sites, presented in figure 10, are generally linear even to quite large zenith angles. All regression coefficients and constants determined for the desert emission models are listed in table IV. The longwave radiant exitance expressed as

$$E_{LW} = \frac{2\pi}{2+M}\bar{L}_{LW,0^\circ} \qquad (12)$$

can be computed from these values.

Discussion of Results

Reflectance Model

Comparisons of the December 1978 and December 1979 Nimbus 7 data for both the Gibson and Saudi Deserts, given in figures 5 and 6, respectively, indicate that there were no significant differences in the levels of the measurements. Therefore, it was assumed that the sensor responses were constant during this period and during the somewhat longer

period of the Sahara data set. Stability is important, particularly for modeling purposes, in that a continuous degradation of the sensors during the December 1978 to July 1979 period, for instance, could have been erroneously incorporated into the models as an effect of θ_0.

The multiaxis ERB scanner obtained measurements for all azimuth angles; however, with the assumption of symmetry about the principal plane, the data for $\phi = 0°$ to 360° were mapped into $\phi = 0°$ to 180° for the binned Sahara data set. Desert sand dunes are usually aligned with the prevailing winds, and this assumption might not be valid for such surfaces. Although the validity of the symmetry assumption could not be assessed for the Sahara data set, there were no significant differences between the measurements for $\phi = 0°$ to 180° and $\phi = 180°$ to 360° for the Gibson and Saudi Deserts.

The regression parameters $Y_0/Y_1, N$, and C_{SW} for the Saudi Desert (table III) were essentially identical for the Nimbus 6 and 7 ERB scanners, but the Y_1 value for the Nimbus 6 was about 9 percent higher than that for Nimbus 7. The inability to determine which of these two values is correct or more nearly correct emphasizes the fact that target sites can only be used to assess long-term sensor stability and not absolute sensor accuracy.

Error sources for the present modeled data include site nonuniformity, instrument noise, meteorological variations, and modeling errors. In spite of such potential errors, the model dispersions (Standard error of the estimate/Mean) were only 5 percent to 8 percent (table III), and site nonuniformities such as those shown in figure 1 could account for a major portion of these dispersions.

All zenith angle terms in the directional model, equation (3), and in the azimuthal phase function, equation (6), appear only in sum or product combinations (i.e., $U + U_0, UU_0$, and VV_0), and therefore, reciprocity exists between the viewing and solar zenith angles. (The values of θ and θ_0 can be switched, and the value of R will be unchanged.) This feature of the target sites allows the present limited range of θ_0 values to be extended to the more extensive present range of θ values. This is a useful feature in that θ_0 will often exceed 50° during passes of the satellite over the sites, and it also lends a degree of confidence to the extrapolated values of the site albedos given in figure 8. The general form of the present model is probably applicable to most deserts and arid regions, and perhaps to other diffuse surfaces.

The stated reason for including the Gibson Desert as an NFOV site was to provide a high-radiance target for the NOAA G scanner from October to March when the solar flux impinging on the surface, SU_0, at the Saudi site would be low. Unfortunately, the albedo of the Gibson Desert is considerably less than that of the Saudi Desert (fig. 8), meaning that its shortwave radiances would exceed those for the Saudi Desert only during December and January. This calculation is based on a nominal 0800 LST equatorial-crossing time, but should the NOAA G spacecraft be launched and/or precess to earlier crossing times, use of the Gibson site would become a necessity.

Unlike the NFOV sensors, the MFOV sensors do not measure radiance, per se, but instead measure radiant flux, F. The shortwave flux can be related in terms of the shortwave radiance as

$$F_{SW} = \int_0^{2\pi} \int_0^{\alpha_{\max}} L_{SW} \sin \alpha \cos \alpha \, d\alpha \, d\beta \quad (13)$$

where α and β are the polar angles of the MFOV sensor. With substitution, this expression becomes

$$F_{SW} = \left(\frac{r_a}{r_s}\right)^2 \frac{SY_1}{\pi} \int_0^{2\pi} \int_{U_{\max}}^1 P_{SW} \left[\frac{Y_0}{Y_1} + \left(\frac{UU_0}{U + U_0}\right)^N\right] dU \, d\beta \quad (14)$$

where r_a and r_s are the earth radii to the top of the atmosphere and to the satellite, respectively. Equation (14) can be numerically integrated by using the scanner-derived regression coefficients to provide an estimate of F_{SW} for the Sahara site.

Emittance Model

The longwave radiance model given by equations (10) and (11) provided good estimates for the noontime Nimbus 6 and 7 ERB measurements, but its regression values, $\bar{L}_{LW,0°}$ and M apply only to noontime and not to other hours of the day. For instance, the noontime values of $\bar{L}_{LW,0°}$ and E_{LW} are quite linear with U_0 for the Sahara Desert (table IV), yet these values are larger in the afternoon than in the morning for the same U_0. The precessing ERBS scanner should provide sufficient longwave measurements to model the diurnal and seasonal variations of $\bar{L}_{LW,0°}$ and M.

The azimuthal anisotropy for the longwave radiances came somewhat as a surprise. However, it should be expected that the side of sand dunes, rocks, and other vertical protuberances facing toward the Sun would be somewhat warmer and thus would emit more energy in that direction than would the opposite side in its direction. These protuberances may also be the major cause of the shortwave anisotropy. (Note that the C_{LW} values given in table IV are an order of magnitude smaller than the C_{SW} values given in table III.) Longwave

anisotropy can be avoided by taking radiance measurements either during nighttime orbital passes after the thermal anisotropy has dissipated or at the nadir ($V = 0, P_{LW} = 1$) during daytime orbital passes.

The MFOV longwave flux for $P_{LW} = 1$ can be expressed as

$$F_{LW} = \left(\frac{r_a}{r_s}\right)^2 \left(\frac{2\pi \bar{L}_{LW,0°}}{2+M}\right)\left(1 - U_{\max}^{2+M}\right) \quad (15)$$

At intervals during the course of the ERBE mission, NFOV scanner measurements of the Sahara site that lie within the fields of view of the MFOV sensors will be modeled to provide the regression coefficients needed for equations (14) and (15). This procedure will provide both shortwave and longwave comparisons between measurements of the NFOV scanner and MFOV sensors. Such comparisons were not possible for ERB because the instrument packages did not have MFOV sensors.

Concluding Remarks

Broadband shortwave and longwave radiance measurements obtained from the Nimbus 7 Earth Radiation Budget (ERB) scanner were used to develop cloud-free reflectance and emittance models for the Sahara, Gibson, and Saudi Deserts. These deserts will serve as in-flight validation targets which, together with onboard calibration systems, will be used to provide radiometric stability for the Earth Radiation Budget Experiment (ERBE) sensors during the course of their mission lifetimes. The large Sahara Desert will serve as the target site for the medium-field-of-view (MFOV) nonscanner sensors. The smaller Saudi Desert will serve as the primary target site for the narrow-field-of-view (NFOV) scanner sensors, with the Gibson Desert as the alternate NFOV site. These deserts were selected as target sites because of their stability, clear skies, high albedos, low latitudes (i.e., low solar zenith angles), size, and uniformity.

The directional reflectance model for these desert sites was a function of sum and product terms of the cosines of the solar and viewing zenith angles, and thus reciprocity existed between these zenith angles. This feature of the sites allows the present limited range of solar zenith angles to be modeled to the more extensive present range of viewing zenith angles. The emittance model was related by a power law of the cosine of the viewing zenith angle. The general forms of both the reflectance and emittance models are probably applicable to most deserts and arid regions, and perhaps to other diffuse surfaces.

NASA Langley Research Center
Hampton, VA 23665-5225
December 5, 1985

References

Barkstrom, Bruce R. 1973: A Comparison of the Minneart Reflectance Law and the Reflectance From a Nonconservative Isotropic Scattering Atmosphere. *J. Geophys. Res.*, vol. 78, no. 27, Sept. 20, pp. 6370–6372.

Barkstrom, Bruce R. 1984: The Earth Radiation Budget Experiment (ERBE). *American Meteorol. Soc. Bull.*, vol. 65, no. 11, pp. 1170–1185.

Harrison, Edwin F.; Minnis, Patrick; and Gibson, Gary G. 1983: Orbital and Cloud Cover Sampling Analyses for Multisatellite Earth Radiation Budget Experiments. *J. Spacecr. & Rockets*, vol. 20, no. 5, Sept./Oct., pp. 491–495.

Sherr, Paul E.; Glasen, Arnold H.; Barnes, James C.; and Willand, James H. 1968: *World-Wide Cloud Cover Distribution for Use in Computer Simulations.* NASA CR-61226.

Short, Nicholas M.; Lowman, Paul D., Jr.; Freden, Stanley C.; and Finch, William A., Jr. 1976: *Mission to Earth: Landsat Views the World.* NASA SP-360.

Smith, W. L.; Hickey, J.; Howell, H. B.; Jacobowitz, H.; Hilleary, D. T.; and Drummond, A. J. 1977: Nimbus-6 Earth Radiation Budget Experiment. *Appl. Opt.*, vol. 16, no. 2, Feb., pp. 306–318.

Staylor, W. Frank 1985: Reflection and Emission Models for Clouds Derived From Nimbus 7 Earth Radiation Budget Scanner Measurements. *J. Geophys. Res.*, vol. 90, no. D5, Aug. 20, pp. 8075–8079.

Stowe, Larry L. 1983: Validation of Nimbus-7 Temperature-Humidity Infrared Radiometer Estimates of Cloud Type and Amount. *Adv. Space Res.*, vol. 2, no. 6, pp. 15–19.

Stowe, L. L.; and Fromm, M. D. 1983: *Nimbus-7 ERB Sub-Target Radiance Tape (STRT) Data Base.* NOAA Tech. Memo. NESDIS 3, National Oceanic & Atmospheric Administration, Dec. (Available from NTIS as PB84 149 921.)

Suttles, John Timothy 1981: Anisotropy of Solar Radiation Leaving the Earth-Atmosphere System. Ph.D. Diss., Old Dominion Univ., May.

Taylor, V. Ray; Stowe, L. L.; and Vilardo, J. M. 1983: Nimbus-7 ERB Reflectance Models for ERBE Processing. *Fifth Conference on Atmospheric Radiation*, American Meteorological Society, pp. 452–455.

Williamson, L. Edwin, ed. 1977: *Calibration Technology for Meteorological Satellites*, First ed. Atmos. Sci. Lab. Monogr. Ser. No. 3., U.S. Army, June. (Available from DTIC as AD A041 662.)

TABLE I. SAHARA DATA BINS

Variable and unit	Data bin ranges
θ, deg	[a]6–15
	15–27
	27–39
	39–51
	51–63
	63–75
	75–87
ϕ,[b] deg	0–9
	9–30
	30–60
	60–90
	90–120
	120–150
	150–171
	171–180
U_0, dimensionless (θ_0, deg)	1.0–0.9 (0–26)
	0.9–0.8 (26–37)
	0.8–0.7 (37–46)
	0.7–0.6 (46–53)

[a]Single-cap bin.
[b]Assumed symmetry about principal plane.

TABLE II. DATA SET RANGES AND POPULATION

Desert site	Spacecraft	θ range, deg	ϕ range, deg	θ_0 range, deg	Number of measurements
Sahara	Nimbus 7	6–87	0–360	0–53	191 bins[a]
Gibson	Nimbus 7	18–85	5–336	4–50	63 points
Saudi	Nimbus 7	6–86	2–356	4–47	62 points
Saudi	Nimbus 6	9–85	1–358	6–20	51 points

[a]Sufficient data were unavailable for 5 of 196 potential bins.

TABLE III. REGRESSION PARAMETERS FOR REFLECTANCE MODEL

Desert site	Spacecraft	Y_0	Y_1	N	C_{SW}	$\sigma/\bar{Y}$
Sahara	Nimbus 7	0.011	0.920	1.764	0.33	0.054
Gibson	Nimbus 7	.009	.623	1.786	.60	.077
Saudi	Nimbus 7	.008	1.088	1.678	.18	.057
Saudi	Nimbus 6	.009	1.186	1.677	.18	.067

TABLE IV. REGRESSION PARAMETERS FOR EMITTANCE MODEL

Desert site	Spacecraft	Time	U_0	C_{LW}	M	$\bar{L}_{LW,0°}$, W/m^2-sr	E_{LW}, W/m^2
Sahara	Nimbus 7	11/78	0.95	0.01	0.144	113	331
		to	.85	.01	.117	107	317
		5/80	.75	.01	.107	101	301
			.65	.01	.095	95	285
Gibson	Nimbus 7	12/78	0.99	0.04	0.170	120	348
		7/79	.65	.04	.121	98	290
Saudi	Nimbus 7	7/79	0.99	0.02	0.164	116	337
		12/78	.72	.02	.148	104	304
Saudi	Nimbus 6	8/75	0.98	0.02	0.176	111	321

1. Report No.	2. Government Accession No.	3. Recipient's Catalog No.
NASA TP-2540		

4. Title and Subtitle	5. Report Date
Site Selection and Directional Models of Deserts Used for ERBE Validation Targets	April 1986
	6. Performing Organization Code: 672-22-04-70
7. Author(s): W. Frank Staylor	8. Performing Organization Report No.: L-16041
9. Performing Organization Name and Address: NASA Langley Research Center, Hampton, VA 23665-5225	10. Work Unit No.
	11. Contract or Grant No.
12. Sponsoring Agency Name and Address: National Aeronautics and Space Administration, Washington, DC 20546-0001	13. Type of Report and Period Covered: Technical Paper
	14. Sponsoring Agency Code

15. Supplementary Notes

16. Abstract

Broadband shortwave and longwave radiance measurements obtained from the Nimbus 7 Earth Radiation Budget scanner were used to develop reflectance and emittance models for the Sahara, Gibson, and Saudi Deserts. These deserts will serve as in-flight validation targets for the Earth Radiation Budget Experiment being flown on the Earth Radiation Budget Satellite and two National Oceanic and Atmospheric Administration polar satellites. The directional reflectance model derived for the deserts was a function of the sum and product of the cosines of the solar and viewing zenith angles, and thus reciprocity existed between these zenith angles. The emittance model was related by a power law of the cosine of the viewing zenith angle.

17. Key Words (Suggested by Authors(s))	18. Distribution Statement
Earth Radiation Budget Desert radiation models Shortwave and longwave radiation Sensor validation targets Nimbus 6 and 7 ERB	Unclassified—Unlimited Subject Category 47

19. Security Classif.(of this report)	20. Security Classif.(of this page)	21. No. of Pages	22. Price
Unclassified	Unclassified	13	A02

For sale by the National Technical Information Service, Springfield, Virginia 22161

NASA-Langley, 1986

National Aeronautics and
Space Administration
Code NIT-4

Washington, D.C.
20546-0001

BULK RATE
POSTAGE & FEES PAID
NASA
Permit No. G-27